Process Development for the Laser Powder Bed Fusion of WC-Ni Cermets Using Sintered-Agglomerated Powder

Edgar Mendoza Jimenez[1], B. Reeja-Jayan[1], Jack Beuth[1]

[1]*Department of Mechanical Engineering, Carnegie Mellon University, Pittsburgh PA 15213*

Abstract

Although ceramic particle-metal matrix materials (i.e. cermets) can offer superior performance, manufacturing of these materials via conventional means is difficult compared to the manufacturing of metal alloys. This study leverages the laser powder bed fusion process to additively manufacturing dense WC-17 wt.% Ni composite specimens using a novel spherical, sintered-agglomerated composite powder. A range of processing parameters yielding high density specimens were discovered using a sequential series of experiments comprised of single bead, multi-layer, and cylindrical builds. Cylinders with a relative density >99% were fabricated and characterized in terms of microstructure, chemical composition, and hardness. SEM images show favorable wetting between the nickel binder and carbide particles without any phase segregation and laser processing increased the average carbide particle size. EDX and XRD analyses detected traces of secondary products after laser processing. For samples processed at high energy densities, complex carbides and carbon agglomerate phases were detected. A maximum hardness of 60.38 Rockwell C is achieved in the printed samples. The successful builds in this study open the way for laser powder bed fusion of dense WC-Ni parts with a large workable laser power-laser velocity processing window.

KEYWORDS: Cermet, WC-Ni, Laser Powder Bed Fusion, Selective Laser Melting

Introduction

Novel applications in the tooling and machining industries drive material development beyond that of established metal alloys to ceramic particle-metal matrix composite (i.e. cermet) material systems [1]. Although cermet materials can offer superior performance (e.g., high temperature resistance, corrosion resistance, and wear resistance), their manufacturing via conventional means is difficult compared to the manufacturing of metal alloys. Traditional manufacturing methods, such as milling and casting, are not suited for materials with high hardness values and melting temperatures. As such, pressing and extrusion methods are used to produce green parts that are subsequently heat treated to create stronger, denser parts. The geometries of these parts are significantly constrained due to the inherent limitations of their fabrication processes. The emergence of additive manufacturing processes presents an opportunity to fabricate ceramic and cermet parts with greater geometric complexity [2][3][4].

Carbide particle-metal matrix or cermets are materials comprised of ceramic carbide particles (e.g., WC, Sic, and TC) homogeneously dispersed within a metal matrix phase. Compared to metal alloys, cemented carbides can exhibit a wide range of thermal/electrical conductivities, abrasion resistance, creep resistance, and stiffness; such properties can be tailored by changing carbide particles, metal matrices, or the ratio between the two phases [5]. Tungsten Carbide (WC) particles are commonly used in cermets; these composites are specifically favored for applications requiring high hardness, temperature stability, tailored thermal and/or electrical conductivities, and wear resistance [6][7]. Mechanical properties of WC cermets are greatly affected by the volume ratio between the metal and WC phases and the size of the carbide grains [8][9]. Cobalt (Co) is typically used as the metal matrix in WC cermets for high strength applications, but nickel (Ni) is

a common substitute as it is less magnetic, exhibits greater corrosion and oxidation resistance, and possesses comparable mechanical properties [10][11].

Many processes can produce WC-Ni composites, but only a few are proven at the industrial level as challenges include economic considerations, powder properties, and powder processability. Bulk WC-Ni parts are typically fabricated using liquid phase sintering techniques where WC and Ni powders are pressed and shaped to a desired geometry. The compacted green part is then subjected to high temperatures (>1300ºC) and pressures (>1 MPa) where the metal melts, wets the WC powder, and densifies the part [12]. WC-Ni coatings can be fabricated by laser cladding methods; in such processes, a laser (typically a CO_2) heats the powder and melts the nickel to generate a coating on a metal substrate. Acker et al. was able to deposit thick layers of WC-Ni with porosities less than 2% and a maximum nickel volume percentage of 45% although nickel agglomerations began to form at volume percentages higher than 30% [8]. High-frequency induction-heated sintering [13], microwave sintering [14], and spark plasma sintering [15] also demonstrate potential to fabricate WC-Ni composites.

Conventional manufacturing techniques demand a great deal of time and energy to produce WC-Ni parts. Additive manufacturing provides a wide collection of processes that can be used to produce geometrically complex, bulk cermets at lower energy and capital costs [16]. Enneti et al. studied the binder jetting capabilities of WC cermets and provided details about sintering densification and mechanical properties. In these studies, an intermediate green part was additively manufactured and post processed in a high temperature (>1400ºC), high pressure sintering step to achieve high densities with high levels of shrinkage [14][15]. The directed energy deposition process has been used to manufacture WC composites, as exemplified by Balla et al. where WC-12% Co dense coatings were deposited onto a steel substrate [19]. The electron beam melting

process has also been used to fabricate WC cermets; Kenyoshi et al. demonstrated the feasibility of printing WC-Co which resulted in specimens with intense WC grain growth due to the high powder bed temperatures of the electron beam melting process [20].

Laser powder bed fusion (LPBF) or selective laser melting (SLM) has advantages over other manufacturing processes because it operates at substantially lower temperatures and can create fully dense, near net shape parts. In this process, a laser beam provides the thermal energy to melt and fuse a thin layer of metal powder in the shape of the cross section of the part. The build platform is then lowered and a new layer of powder is deposited, usually by a recoater blade dragging powder from a dispenser platform to the build platform. Several studies explore the possibilities of printing WC-Co cermets with LPBF: Uhlmann et al. measured porosity and cobalt content of printed samples [21], Khmyrov et al. demonstrated the possibility of printing with nano-sized WC powder [22], Campanelli et al. analyzed the resulting microstructure of Cr-doped WC-Co builds [23], and Kumar achieved high density prints using a WC-Co composite powder [24]. Ku et al. examined the feasibility of printing cemented WC with an iron alloy matrix (10 wt.%) and printed samples with densities up to 95% and macropores as big as 500 microns [25]. Kang et al. printed miraging steel with up to 15 wt.% WC and found an increase in WC decreased the surface roughness, increased ultimate tensile strength, increased repeatability of processing, increased thermal conductivity and created a more homogenous samples [26]. Cavaleiro et al. conducted a study on surface modified WC particles to print a WC cermet reinforced with steel [27].

The LPBF of WC-Ni cermets, our material system of interest, was reported in several studies. Gu et al. processed in situ WC-Ni based cemented carbides using a mechanically mixed W-C-Ni ternary powder system in the LPBF process [28][29]; this approach resulted in samples

with a maximum relative density of about 96% and the formation of unwanted complex carbides that can compromise mechanical strength. In another study, Li et al. investigated the solidification process of nickel-coated W_2C-WC powder in the LPBF process[30]; this approach produced specimens with carbide grains larger than what's typically desired (0.5-15 μm [1]), phase segregation between carbides and nickel binder, and a significant amount of unwanted complex carbides. The novelty of this work focuses on introducing a new type of powder to process WC-Ni within the laser powder bed fusion process.

In this study, we additively manufacture cemented WC with a nickel matrix (17 wt.%) using a spherical, sintered and agglomerated WC-Ni composite powder. A 17wt% was chosen because it's the largest amount of metal content offered by the powder manufacturer. This powder, coupled with careful processing parameter selection, can be leveraged to improve some of the most common, and previously mentioned, issues in the LPBF of cemented carbides: inhomogeneity or phase segregation between the metal matrix and ceramic particles, poor powder flowability, low powder bed packing efficiencies, low printed densities, large amounts of unwanted products after laser processing, and poor wetting between carbide particle and metal binder. A series of experiments based on sequential prints is used to discover a range of workable processing parameters for this powder. Process outcomes (e.g., density/porosity, microstructure, chemical composition, and hardness) are evaluated and correlated with processing parameters. As such, the successful builds in this study clearly open the way for the fabrication of fully dense and functional WC-Ni parts, via the laser powder bed fusion process.

Experimental Methods

a) Materials

304 stainless steel build plates were used for each build. The powder used in this study is a sintered and agglomerated WC-Ni composite powder (WOKA 3502) manufactured and supplied by Oerlikon Metco (Switzerland) with the intended purpose of being used for thermal spray coatings. The powder underwent scanning electron microscopy (SEM) with a back scattering electron (BSE) detector, which will make the heavier tungsten element appear brighter than the lighter nickel element. Images of the powder (Figure 1) show the particles are composed of fine (~1 µm, measured using the line intercept method) WC particles within a darker nickel matrix. The powder particles have an average diameter of 30 µm, a D10 value of 10 µm, and a D90 value of 45 µm. Given its size distribution and spherical shape, the powder exhibits superior flowability and a high packing efficiency during layer deposition, which is necessary to build high density parts in the LPBF process [31][32]. Because the carbide grains are homogeneously embedded within the powder's metal matrix, there will be no segregation of phases in the powder bed; this should allow for better wetting of the WC particles and mitigate the production of metal deposits within the printed part after laser processing. The powder was not preprocessed before printing.

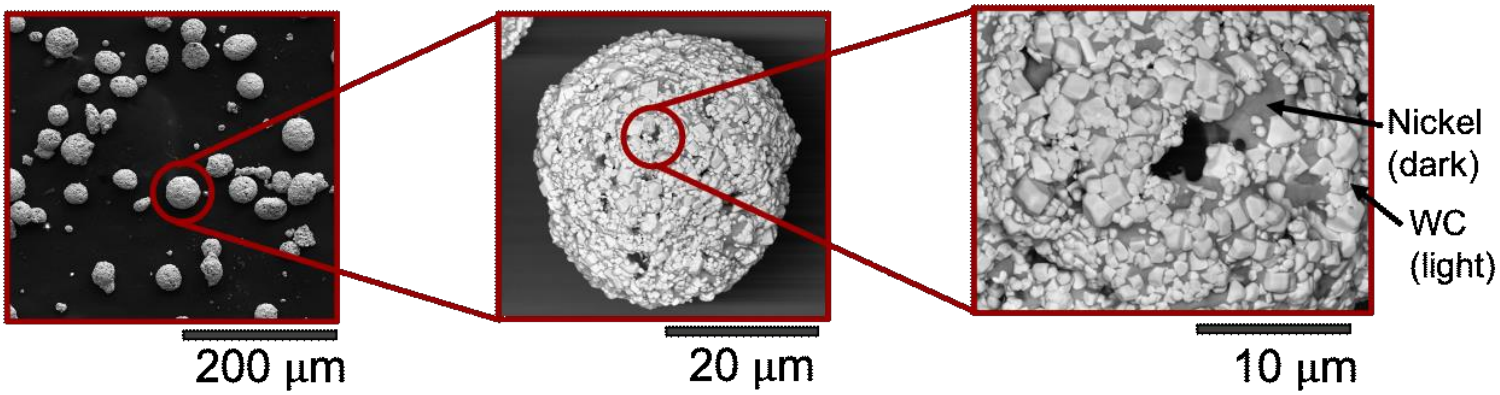

Figure 1: Scanning electron microscopy images of WC-Ni composite powder. WC and nickel phase are shown light and dark grey, respectively. Powder is spherical in shape and posseses fine (<1µm) WC particles uniformly distributed throughout the powder agglomerate.

b) Fabrication Process

Experiments were performed on an EOS M290 (EOS GmbH, Germany) LPBF machine at Carnegie Mellon University's NextManufacturing Center. The machine is equipped with a neodymium-doped ytterbium-aluminum garnet (Nd:YAG) laser with a wavelength of 1.07 µm and maximum power output of 400 W. The laser spot diameter is approximately 100 µm at the top surface of the powder bed. The build plate measures 250 mm x 250 mm and the build volume extend to 325 mm in height. At the start of the build, argon floods the build chamber and continuously flows across the build area; laser processing will occur if oxygen concentration within the chamber is less than 1000 ppm. The only heating in the system originates from the preheated build plate; a build plate temperature of 200 ºC, which is the highest temperature capable by the EOS M290, is chosen to maximize the number of laser power-laser velocity combinations that will fully melt the powder. A brush recoater is used, as opposed to a blade recoater, because it can adapt to a part's thermal deformation. This lowers the probability of the recoater jamming, shearing off the part, and/or interrupting the build.

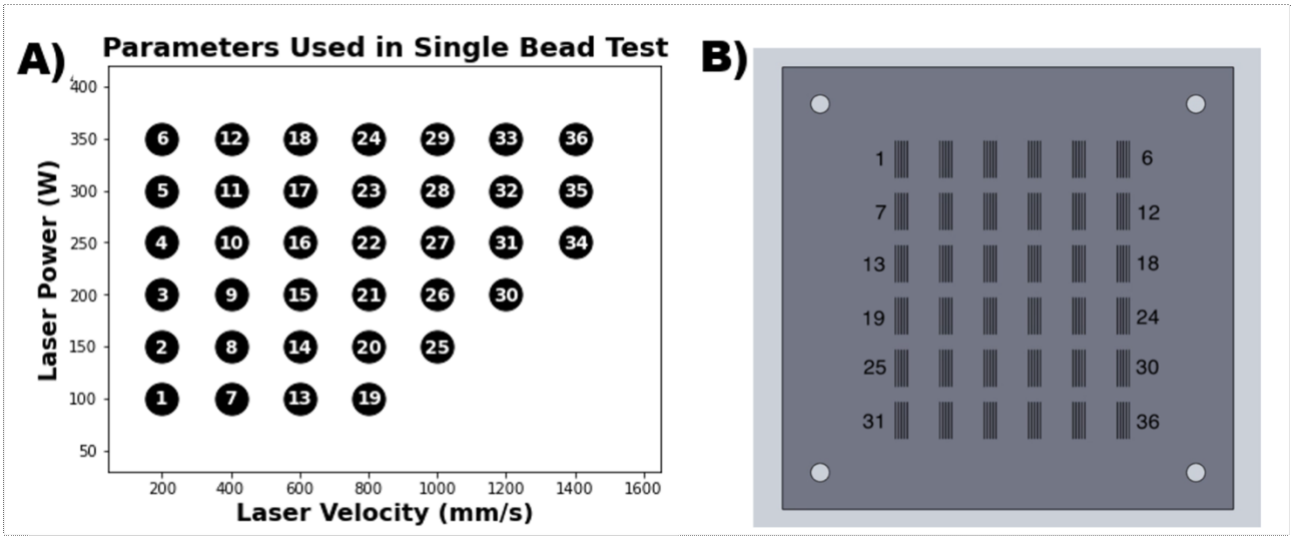

Figure 2: A) Laser power and laser velocity combinations used in the single bead experiment and B) their respective location on the build plate.

c) Fabrication Procedure

The procedure to identify a suitable processing region for WC-Ni powder can be broken up into three sequential experiments: a single bead/track build, a multilayer/pad build, and a specimen build. The single bead experiment was used to evaluate the powder's melting behavior and dimensions of the solidified bead. The multilayer/pad experiment was used to evaluate porosity of the pads and any delamination effects between pad and build plate. The final specimen build was used to evaluate density/porosity, chemical composition, microstructure, and mechanical properties (i.e. hardness).

In the single bead experiment, 36 laser power and laser velocity combinations were used to print five beads each (as seen in **Figure 2**). Typically, single bead printing parameters can be chosen by modelling the melted region using an Eager-Tsai model and the material's thermal properties [33]. However, thermal and absorptivity properties are unknown for this material. In a similar situation, previous authors took an approach in choosing parameter combinations based on work that investigated the variability in melting behavior and morphology of a nickel-based alloy [34]. Beads were printed at 1 cm length to ensure steady state thermal conditions. One layer of powder was deposited with a layer thickness of 50 μm. To mitigate the effects of residual heating by adjacent beads, the order of exposure for the beads were arranged such that a minimum of two seconds elapsed between adjacent beads. Distance between adjacent beads was 1 mm, which avoids the denudation of powder [35] .

In the pad experiment, the processing region was reduced based on the single bead experiments. Eighteen parameter combinations were selected to print one-centimeter squares consisting of ten layers. Each pad had a normalized hatch spacing of 0.7 times the measured width of its respective single bead. Scan rasters were rotated 67º at every layer. To mitigate the effects

of residual heating by adjacent pads, the order of exposure for all the pads was arranged such that a minimum of 5 seconds elapsed between adjacent pads.

The parameter combinations that successfully built pads were used to print 15 mm tall cylinders with a diameter of 15 mm. Scan rasters were again rotated 67º at every layer. To mitigate the effects of residual heating by adjacent pads, the order of exposure for all cylinders was arranged such that a minimum of 5 seconds elapsed between adjacent samples. To mitigate the effects of residual heating by the previous layer, a minimum of 60 seconds elapsed between layers.

d) Characterization

Beads were topographically imaged with an Alicona Infinite-Focus optical microscope. The melting behavior of each parameter combination was manually classified as full/acceptable melting (bead is continuous with constant width), partial melting (bead is discontinuous or has inconsistent width), or no melting (bead does not appear). Widths for continuous beads were measured using line intercept methods via ImageJ. Approximately twenty measurements were taken for each continuous bead to ensure a high confidence measurement.

Pads were cross sectioned on the sacrificial build plate via electric discharge machining (EDM). Sample preparation was conducted per ASTM B665 [36]; cross sectioned samples were hot mounted and polished down to 1 μm using diamond suspension. The cross section of each pad was optically imaged (Alicona microscope). These images underwent a particle analysis to quantify the apparent porosity of each processing combination using ImageJ per ASTM B276 [37]. Relative densities were calculated as the inverse of the apparent porosity.

Cylinders were removed from the build plate and cross sectioned via EDM. Sample preparation was conducted per ASTM B665 [36]; cross sectioned samples were hot mounted and

polished down to 1 μm using diamond suspension. Relative density for each cylinder was measured the same way the pads were. Scanning Electron Microscopy (SEM) and Energy Dispersive X-Ray (EDX) Analysis were performed in a Quanta 600 microscope using a back-scattering detector at an operating voltage of 15kV and a working distance of 10.5 mm. X-Ray diffraction (XRD) was carried out on polished samples to determine the chemical composition (PANalytical X'Pert Pro, United Kingdom); diffraction patterns were collected with 2θ steps of 0.02º and 120 μs of acquisition time. The macrohardness of each printed specimen was measured on the Rockwell C (HRC) scale using a Wilson Rockwell 2000 Hardness Tester per ASTM E18 [38]. For these tests, a one cm square with a minimum thickness of 5 mm was sectioned out of each cylinder via EDM. Ten measurements were carried out at different locations for each sample.

Results and Discussion

a) *Single Beads (SB)*

The laser power and laser velocity combinations resulted in beads that were fully melted, partially melted, and not melted. Classification of each parameter combination is shown in **Figure 3A**. As expected, the melting behavior diminishes as the energy density decreases, which suggests the top left of the processing space would be optimal to work in. Each laser power-laser velocity combination and its respective label was used to train a logistic regression model. This model interpolated and extrapolated melting behavior across the processing space and is shown in **Figure 3A** and **3B** where the green region predicts full melting of the powder, the yellow region predicts partial melting of the powder, and the blue region predicts no melting of the powder.

Bead width measurements for all continuous single beads are shown in **Figure 3B** as a function of laser power and laser velocity. A large range of bead sizes can be produced by simply adjusting the laser power and laser velocity; the largest bead had an average width of 246 µm, and the minimum bead width for our material system is about 130 µm. Consistent with results seen in

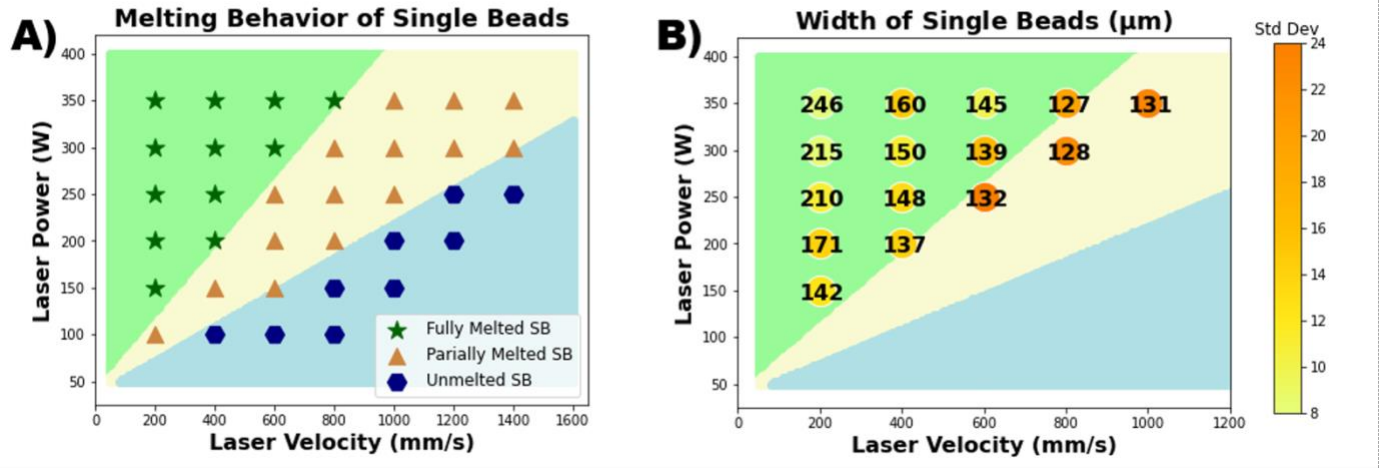

Figure 3: A) The melting behavior of each laser power and laser velocity combination based off the single bead (SB) experiments superimposed over the predicted melting behavior. B) The widths and standard deviations of the continuous single beads superimposed over the predicted melting behavior. For both plots, full melting is expected in the green region, partial melting in the yellow region, and no melting in the blue region.

The laser power and laser velocity combinations used to print the pads are shown in **Figure 4A** with the measured relative densities on each point. Optical images of various cross sectioned pads on the substrate are shown in **Figure 4B**, and the respective parameter combination of each pad is labeled to the right of its measured density in **Figure 4A**. Increasing the energy density increases the resulting relative density of the pad, because a higher energy density increases the size of the region of melted Ni, ensuring very little of the matrix goes unmelted. Large pores were present in pads built in or near the "partially melted" processing space (cross sections A and D in **Figure 4B**); such pores originate due to insufficient melting of the Ni within the composite powder or insufficient overlap between adjacent melt tracks. Pads in the top left of the processing space reached nearly full density (>99%) as shown in cross sections B and C in **Figure 4B**). Pads that achieved >99% relative density operate in the processing space that would result in keyholing porosity of pure nickel alloys, as seen in Scime et al. [34]. This suggests that the addition of carbide particles mitigates the formation of keyholing porosity, perhaps by mitigating the formation of a

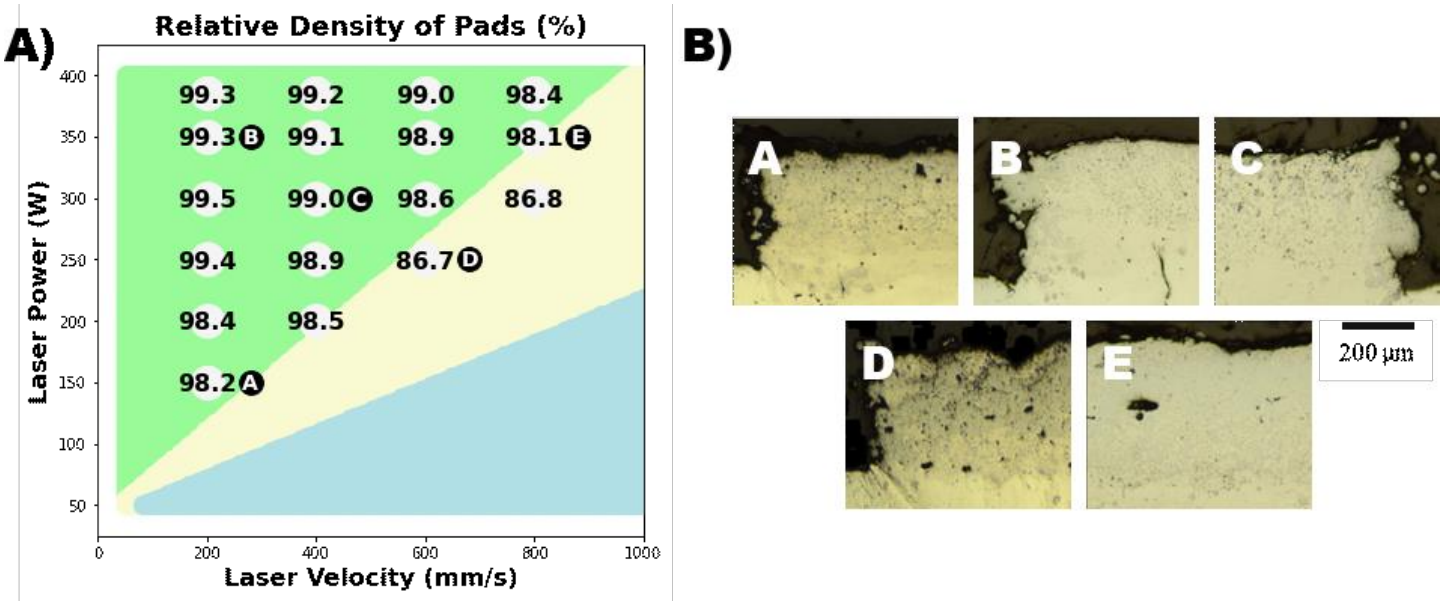

Figure 4: A) Resulting relative densities of pads as a function of laser power and laser velocity superimposed over the predicted melting behavior of the powder; full melting is expected in the green region, partial melting in the yellow region, and no melting in the blue region. B) Optical images of cross sectioned pads from various locations in the processing space.

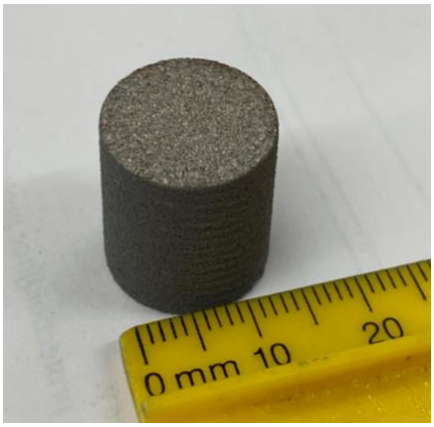

Figure 5: WC-Ni cylinder specimen removed from build plate

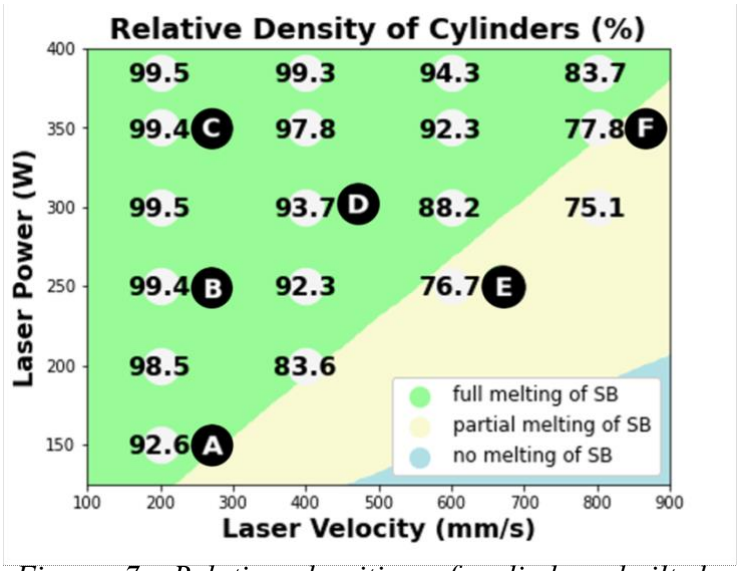

Figure 7: Relative densities of cylinders built by processing parameter combinations superimposed over the melting behavior of the powder evaluated from the single bead (SB) experiment.

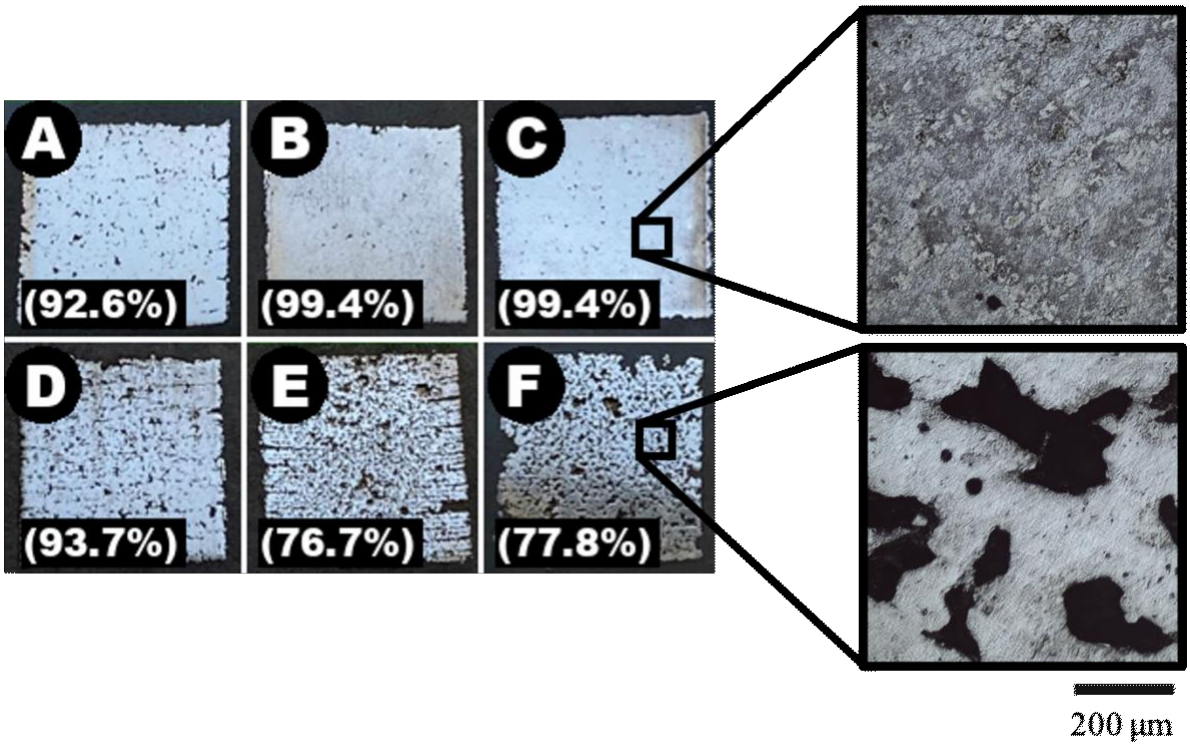

Figure 6: Cross sectional images of samples built by various processing parameters (Figure 6). Relative densities are labeled at the bottom of each image. Porosity visibly decreases when increasing the laser power and decreasing the laser velocity. Magnified images of cross section C and F are presented. Cross section C shows a highly dense sample, while cross section F demonstrates large pores caused by lack of fusion.

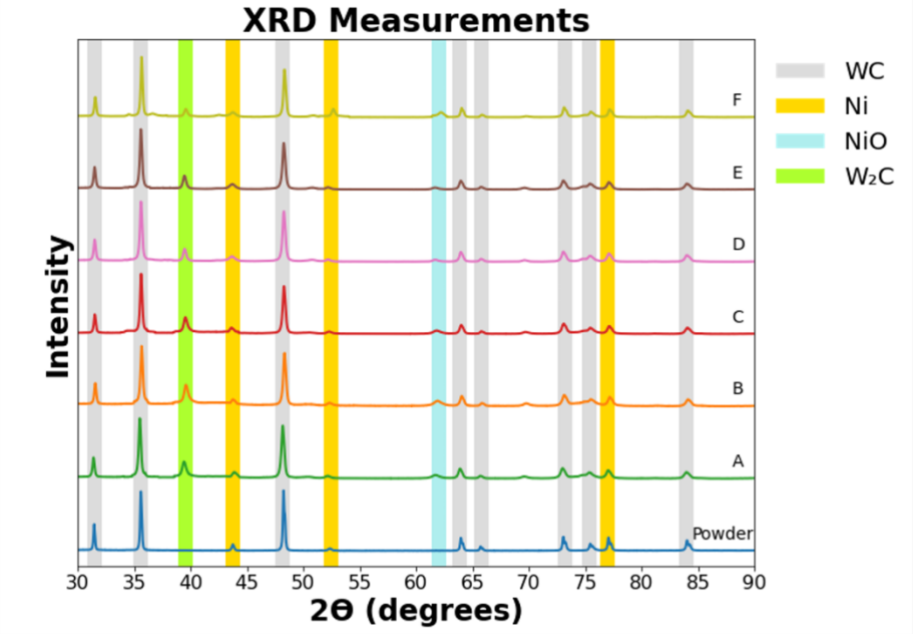

Figure 8: XRD analyses of samples built by various processing parameters (Figure 6). WC and Ni phases are present for all printed specimens. Laser processing also produced unwanted products (e.g., NiO, and W_2C) not present in the original powder.

deep vapor channel caused by the vaporization of the nickel. Although cracks did not form within the printed pads, crack formation and keyholing porosity was observed within the steel build plate, near the pad-substrate interface, at high energy dense processing combinations. Fortunately, these defects within the substrate did not result in the delamination of the printed pads.

c) Cylinders

In an initial cylinder build, the recoater blade impacted some specimens as it moved across the powder bed to deposit a new layer of powder. These impacts caused a few cylinders to shear off the build plate. To overcome this type of build failure, the layer thickness was increased by 40% to 70 µm. Increasing the layer thickness increases the clearance between the blade the top surface of the part, ensuring no impact would occur. All cylinders were printed successfully after this parameter modification (**Figure 5**).

Measured relative densities are labeled over the cylinder's parameter combination in **Figure 6.** The process parameters used in the fabrication of the cylinders produced specimens with a relative density range between 83.4-99.5%. The maximum density in this build is higher than those reported in previous LPBF WC-Ni studies [28–30]. Several sectioned and polished specimens from different locations in the processing space (as indicated in **Figure 6**) are shown in **Figure 7**. Lack-of-fusion porosity appears to be the main mechanism behind the resulting porosity of the printed samples, similar to that of metal alloys [40]; This porosity is reduced by increasing laser power or decreasing the laser speed, which ultimately increases the size of the melt pool and the overlap between meltpools to ensure more of the material is melted and resolidified. A magnified image of Sample F (**Figure 7**) exemplifies the large pores that result from lack of fusion. These pores are not found in highly dense samples, as seen in magnified images of Sample C (**Figure 7**). Upon inspection, relative densities of the cylinders decreased from those of the pads, likely because more energy is needed to melt the larger amount of material caused by the increase in layer thickness. The increase in layer thickness increases the slope of the "partial melting" threshold, which further reduces the "acceptable melting" processing region.

XRD spectra (**Figure 8**) confirm all WC and nickel peaks from the powder are still present in the six specimens. However, W_2C and NiO peaks are present in the printed samples but are not present in the powder, which indicates laser processing causes a compositional change to the material system. The growth of a W-rich phase (W_2C) is common in other WC processing methods and can be attributed to the thermal degradation of the WC particles [41]. The NiO phase is produced by the oxidation of the Ni phase since there may still be traces of oxygen inside the chamber during laser processing.

SEM image of a cylinder's microstructure and its respective EDX chemical mapping are shown in **Figure 9**, and specific point measurements from the image are shown in **Table 1**. EDX mapping qualitatively shows a strong contrast between Ni and W phases; WC particles are lighter, and a darker Ni fills the space within the particles in the SEM micrograph. The carbon is evenly distributed throughout the WC grains, and oxygen shows no preference. A small number of pores between the WC particles and nickel phases suggests sufficient melting of the nickel and wetting of the WC particle; the heating cycles allowed for (1) the melting of the nickel, (2) fluid flow and rearrangement, and (3) solidification. WC particles are homogenously distributed throughout all the samples. For each printed sample, hundreds of carbide particle sizes were measured using the line intercept method on SEM micrographs. **Figure 10** shows the average particle size and standard deviation for each laser power-laser velocity combination. Laser processing induces an increase in carbide particle sizes from the average of 1 μm (present in the powder) to a value that appears to be directly correlated to the laser's energy density. The largest average particle size achieved in this study was 2.61 μm and occurred at a power of 375W and velocity of 200 mm/s. The presence of grain growth and an increase in particle sizes suggests the laser energy is high enough to create a wet film around the WC particles and recrystallize them together, a phenomena also observed in high-temperature spraying techniques [6][25].

Samples with very high laser powers and low laser velocities (i.e., high energy densities) showed additional phases within its microstructure and more exaggerated grain coalescence (**Figure 11**). Dendritic-like grains are present in between the WC particles. Chemical mapping (**Figure 11**) and specific point measurements (**Table 2**) show these complex grains are solid solution phases composed of Ni, W, and C and can be labeled as a complex Ni(W,C) phase; these phases are known to be brittle in nature and detrimental to the cermet structure because they

decrease the amount of metallic binder [42]. Specimens built at high energy densities are also plagued with "dark spots" throughout their microstructure, which are shown to be carbon agglomerates by the EDX mapping and point measurements (**Table 2**). It is often difficult to identify these new phases in the XRD measurements (**Figure 8**), because their characteristic peaks are often broadened, convoluted, and/or shifted [43].

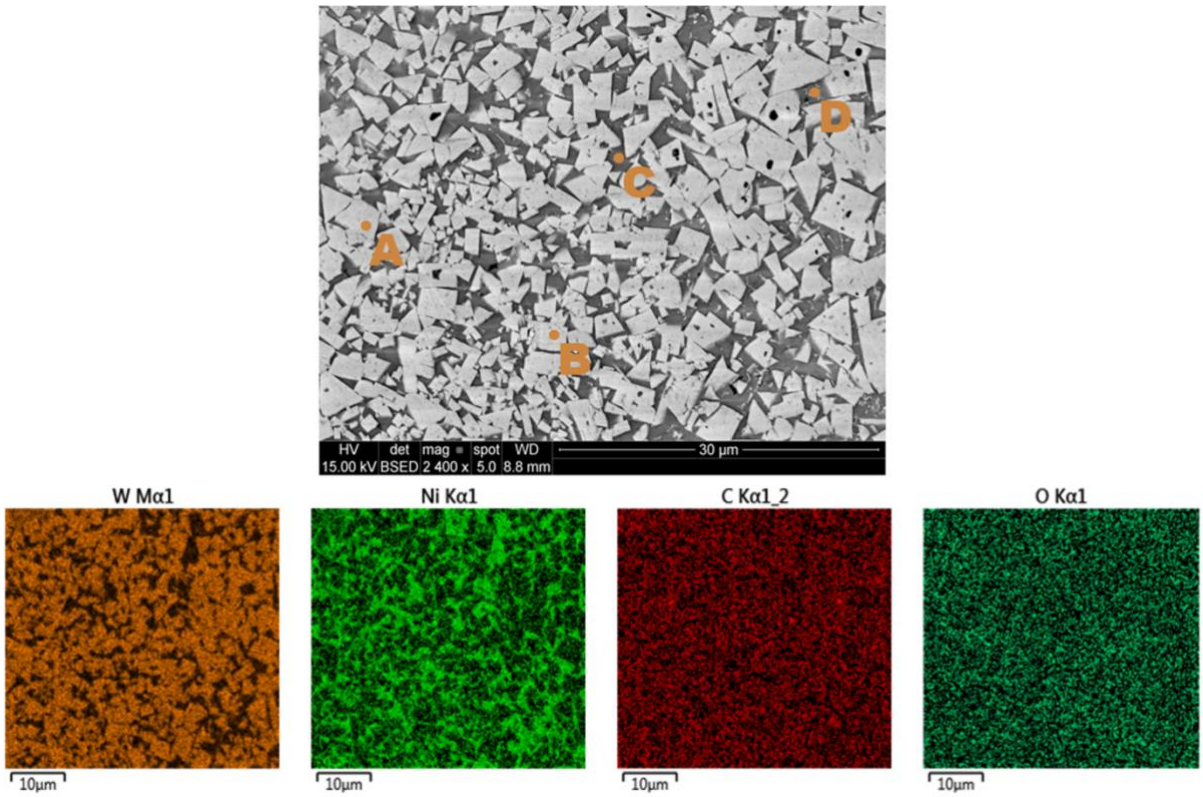

Figure 9: SEM image of typical microstructure found in all specimens shows good wetting of nickel binder as it surrounds the WC particles. EDX chemical composition maps are shown for elements of interest (W, Ni, C, O). W and C are present in the carbide particles (light grey), while Ni is predominantly in the matrix phase (dark grey). Oxygen shows no preference within the microstructure.

	A	*B*	*C*	*D*
W atomic %	53.2	53.4	11.4	13.4
C atomic %	40.0	41.2	4.8	3.4
Ni atomic %	3.6	2.4	82.2	81.5
O atomic %	3.2	3.0	1.6	1.7

Table 1: EDX point measurements showing chemical compositions at various locations within the microstructure of printed samples, as seen in Figures 9.

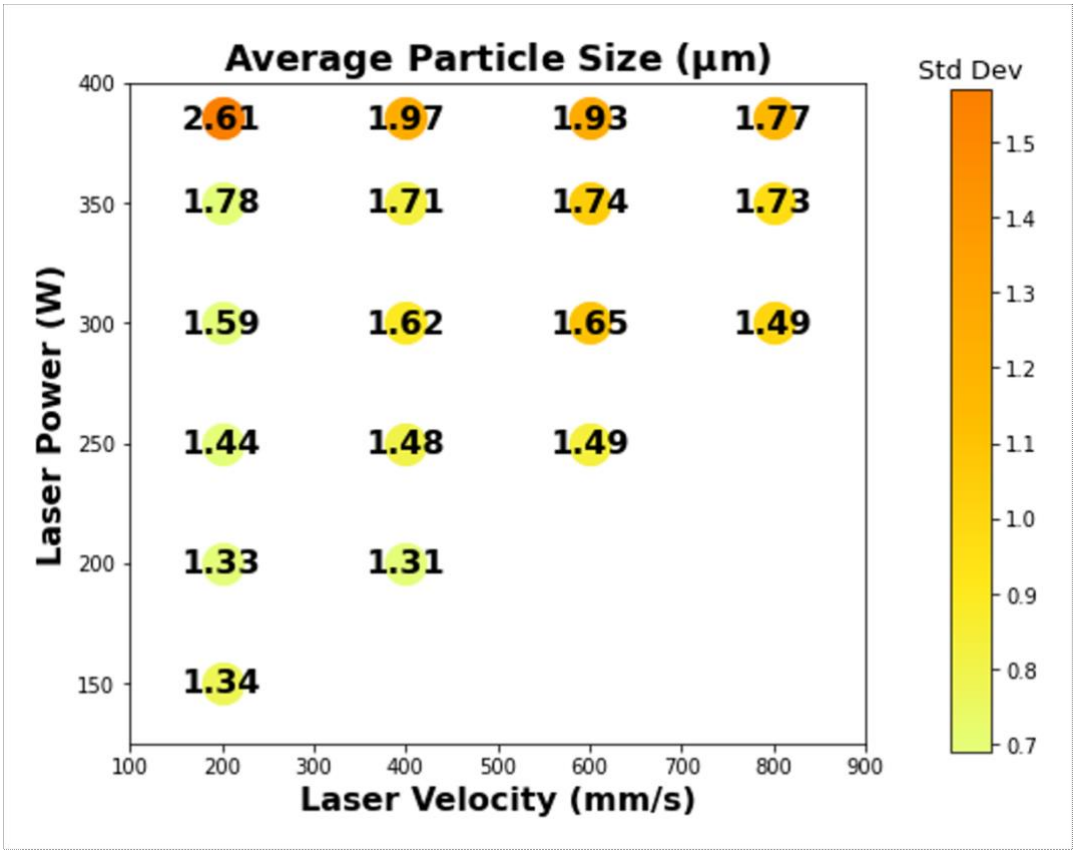

Figure 10: Average particle size and respective standard deviation of printed cylinders projected onto the processing space as a function of laser velocity and laser power. Average particle size generally increases with increasing energy density.

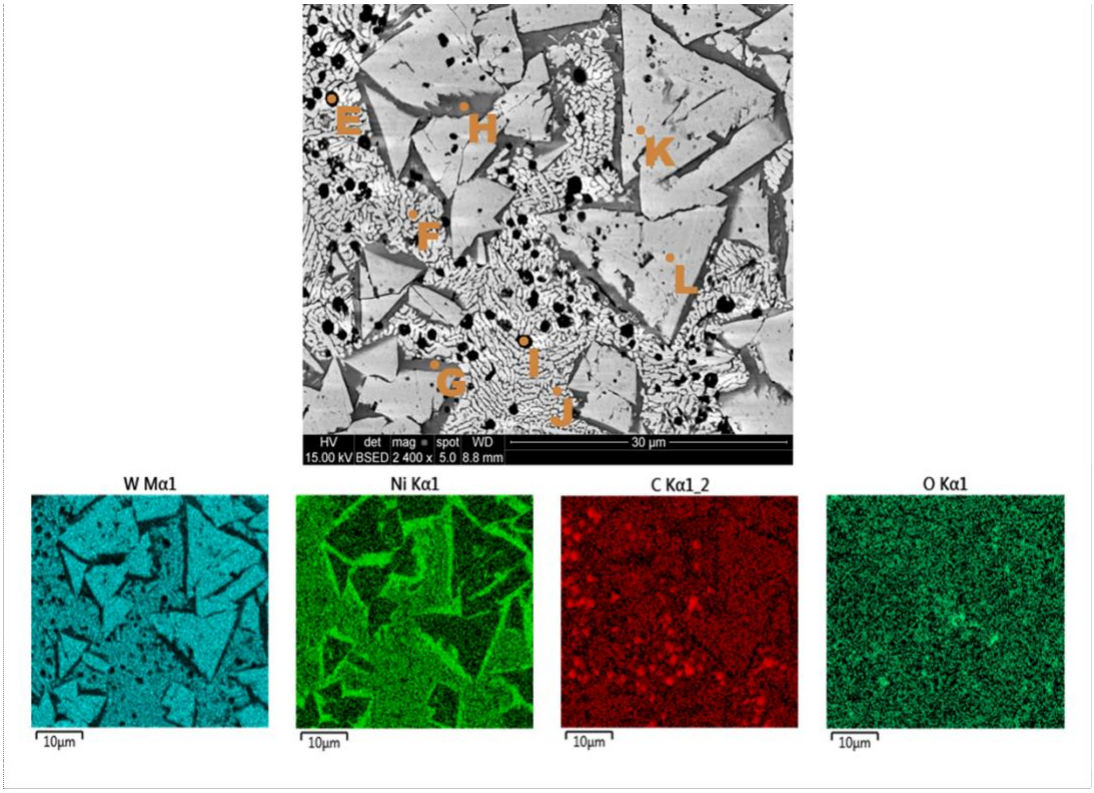

Figure 11: SEM image of microstructure found in the specimen processed with the highest energy-dense processing parameters. Light grey carbide particles and dark grey nickel matrix are present. However, novel dendritic-like and agglomerate-like phases are also present in these samples. EDX chemical composition maps are shown for elements of interest (W, Ni, C, O). The dendritic-like phase contains W, Ni, and C so it can be labeled as a complex carbide. The dark agglomerates contain mostly C.

	E	***F***	***G***	***H***	***I***	***J***	***K***	***L***
W atomic %	4.3	68.1	10.0	7.7	3.4	59.7	54.6	53.1
C atomic %	86.9	17.4	4.4	3.9	90.6	16.7	39.9	40.5
Ni atomic %	8.6	12.5	83.1	86.7	5.7	20.3	3.2	3.2
O atomic %	0.2	2.0	2.4	1.7	0.3	3.3	2.3	3.2

Table 2: EDX point measurements showing chemical compositions at various locations within the microstructure of printed samples, as seen in Figures 9.

Regardless of process parameters, all point measurements done on WC particles showed a noticeably greater amount of W compared to C. The imbalance in the atomic composition between tungsten and carbon suggests the formation of W_2C on the surface of the WC particles, a phase that forms at high temperatures (>2700 ºC) and is metastable below 1250 ºC [43]. The presence of W_2C on WC particles, regardless of processing conditions, and the formation of complex Ni(W,C) phases and carbon agglomerates at high energy densities indicate the laser processing produces various degrees of carbide decomposition or decarburization within the printed samples [42]. Decarburization is well documented in the high temperature processing of WC-metal coatings and is characterized by a reduction in WC content and formation of undesirable phases such as W_2C, W, C, and amorphous or nanocrystalline Ni-W-C phases [43,44]. It is hypothesized that the laser processing in this study provides enough energy for the thermal decomposition of tungsten and carbon within the WC particles, as shown in **Figure 12.** If there are traces of oxygen in the system, it's possible the oxygen reacts with the nickel and carbon to form nickel oxide, carbon dioxide, and W_2C (**Figure 12A**). Given their drastically different diffusion rates in melted nickel, the carbon can quickly diffuse out of the carbide and agglomerate to form carbon particles while the slow and heavy tungsten remains in the carbide to form W_2C and, if the temperatures are high enough, react with the nickel to form Ni(W,C) (**Figure 12B**).

Rockwell C hardness measurements of all samples shows the relationship with porosity (**Figure 13A**). Hardness decreases in a logarithmic behavior, and least squares fit of the measurements predicts the relationship between hardness and porosity is

$$Hardness = 55.6 - 4.7 * log(P)$$

where P is porosity (in percentage form). This fit is projected in **Figure 13A** and shows good fit with the measurements. When projected onto the processing space, hardness generally increases

as energy density increases (**Figure 13B**). Although comparing hardness between cermet systems is nontrivial since hardness is dependent on the metal matrix, carbide particle size, and volume ratio between metal matrix and carbide particle, the obtained maximum hardness of 60.38 Rockwell C meets the nominal hardness (60.0 Rockwell C, per vendor's specifications) of thermal spray coatings fabricated from the same powder used in this study. Maximum hardness was achieved with the following processing parameters: 300 W laser power, 200 mm/s laser speed, 70 µm layer thickness. At a laser velocity of 200 mm/s, there was a noticeable decrease in hardness once laser power exceeded 300 W. This decrease can be attributed to the minor decrease in relative density (as seen in **Figure 6)**, increase in carbide particle sizes (**Figure 10**), and/or the increasing presence of novel metallic carbide phases (as seen in **Figure 11**).

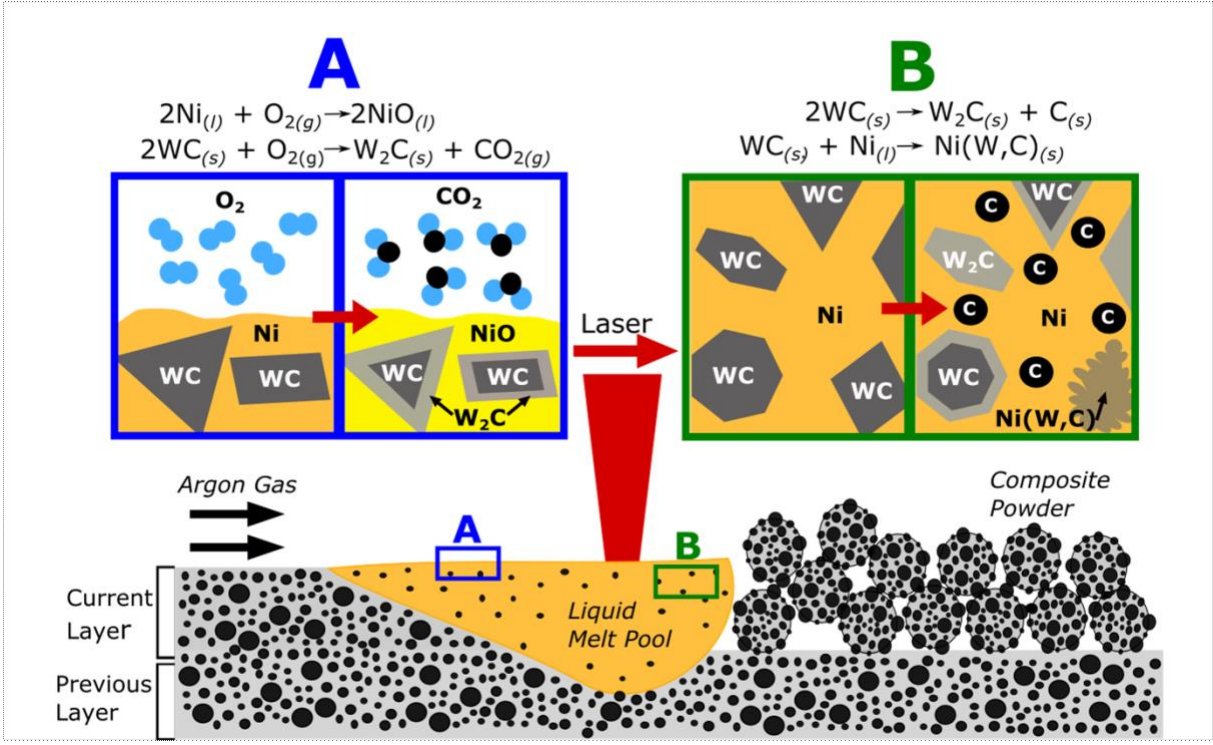

Figure 12: Laser processing of the WC-Ni composite powder can produce several products. (A) If there are traces of oxygen in the chamber, the oxygen atoms can react with the liquid nickel to form liquid NiO and react with the solid carbide to form solid W_2C and gaseous CO_2. (B) The decomposition of W and C within the carbide can cause the formation of W_2C, carbon agglomerates, and a complex Ni(W,C) phase.

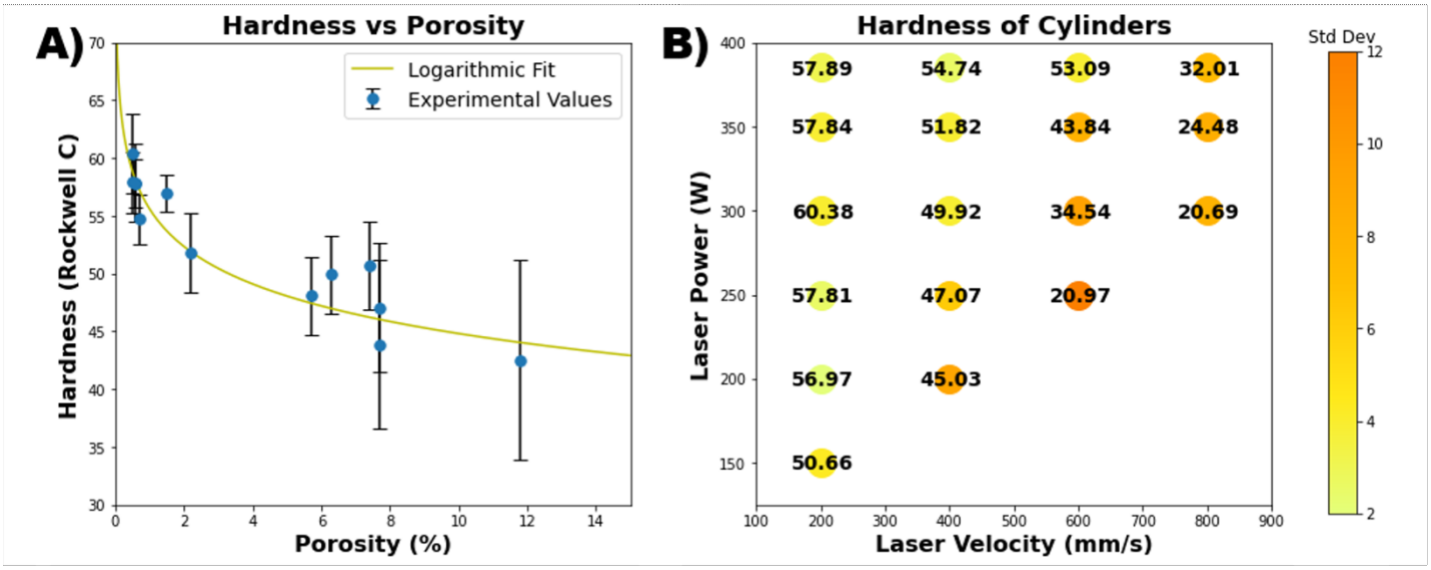

Figure 13: A) Hardness values of printed cylinders plotted against their respective porosity. Hardness is indirectly correlated with porosity and drops drastically when porosity exceed 1%. B) Hardness values of printed cylinders projected onto the processing space as a function of laser velocity and laser power. Hardness generally increases as laser velocity decreases and laser power increases.

Conclusion

In this study, a sintered and agglomerated WC-Ni composite powder with 17 wt.% nickel was processed in a laser powder bed fusion machine. A successive series of experiments was applied across single beads, 10-layer pads, and cylinders (in that order), linking the powder's melting behavior to the successful fabrication of three-dimensional specimens. A region of full melting behavior was found via single bead experiments. The process parameters that produced acceptable melting were used to successfully print pads consisting of ten layers with no delamination from the build plate. The apparent densities of these pads were directly correlated with the energy densities of their respective processing parameters. Highly dense (>99%) cylindrical samples were successfully printed at various processing parameters. XRD chemical analyses indicate WC and Ni phases are present in all printed specimens, and traces of W_2C and NiO are produced after laser processing. SEM images show good wetting between WC and Ni phases and mixing is homogenous without the apparent segregation of phases. However, an increase in decarburization occurs in samples that were processed at high energy densities, resulting in the formation of W_2C on the surface of WC particles, carbon agglomerates, and complex Ni(W,C) phases. Hardness is indirectly correlated with porosity and the relationship appears to be exponential. The maximum hardness value within the printed cylinders (60.38 Rockwell C) is comparable to that of specimens fabricated via conventional means. Parts with the highest densities and hardness were processed with the following processing parameters: 300 W laser power, 200 mm/s laser speed, 70 μm layer thickness. The successful builds in this study clearly open the way for laser powder bed fusion of dense WC-Ni parts without the need for post-processing. These successes appear to be robust given the large workable laser power-laser velocity processing window that prints highly dense WC-Ni cermets, which is constrained by low

energy dense parameters that produce lack-of-fusion porosity and high energy dense parameters that increase carbide particle sizes and decarburize the WC particles to produce unwanted phases.

Acknowledgements

Edgar Mendoza Jimenez acknowledges support from the National Science Foundation (NSF) Graduate Research Fellowship (award number DGE1745016). B. Reeja-Jayan acknowledges support from her NSF CAREER (award number CMMI1751605). The authors acknowledge support from the NextManufacturing Center at Carnegie Mellon University and consortium member John Crane. The authors acknowledge Todd Baer from the NextManufacturing Center for his assistance in handling laser powder bed fusion equipment. The authors would like to acknowledge use of the Materials Characterization Facility at Carnegie Mellon University under grant #MCF-677785.

References

[1] J. García, V. Collado Ciprés, A. Blomqvist, B. Kaplan, Cemented carbide microstructures: a review, Int. J. Refract. Met. Hard Mater. 80 (2019) 40–68. doi:10.1016/j.ijrmhm.2018.12.004.

[2] A. Goulas, R.J. Friel, U. Kingdom, Laser Sintering of Ceramic Materials for Aeronautical and Astronautical Applications, (2017).

[3] D.D. Gu, W. Meiners, K. Wissenbach, R. Poprawe, Laser additive manufacturing of metallic components: Materials, processes and mechanisms, Int. Mater. Rev. 57 (2012) 133–164. doi:10.1179/1743280411Y.0000000014.

[4] E. Mendoza Jimenez, D. Ding, L. Su, A.R. Joshi, A. Singh, B. Reeja-Jayan, J. Beuth, Parametric analysis to quantify process input influence on the printed densities of binder jetted alumina ceramics, Addit. Manuf. 30 (2019). doi:10.1016/j.addma.2019.100864.

[5] A.O. Inegbenebor, C.A. Bolu, P.O. Babalola, A.I. Inegbenebor, O.S.I. Fayomi, Aluminum Silicon Carbide Particulate Metal Matrix Composite Development Via Stir Casting Processing, Silicon. 10 (2018) 343–347. doi:10.1007/s12633-016-9451-7.

[6] Z.Z. Fang, X. Wang, T. Ryu, K.S. Hwang, H.Y. Sohn, Synthesis, sintering, and mechanical properties of nanocrystalline cemented tungsten carbide - A review, Int. J. Refract. Met. Hard Mater. 27 (2009) 288–299. doi:10.1016/j.ijrmhm.2008.07.011.

[7] H. Wang, T. Webb, J.W. Bitler, Study of thermal expansion and thermal conductivity of cemented WC-Co composite, Int. J. Refract. Met. Hard Mater. 49 (2015) 170–177. doi:10.1016/j.ijrmhm.2014.06.009.

[8] K. Van Acker, D. Vanhoyweghen, R. Persoons, J. Vangrunderbeek, Influence of tungsten carbide particle size and distribution on the wear resistance of laser clad WC/Ni coatings,

Wear. 258 (2005) 194–202. doi:10.1016/j.wear.2004.09.041.

[9] H.C. Kim, I.J. Shon, J.K. Yoon, J.M. Doh, Z.A. Munir, Rapid sintering of ultrafine WC-Ni cermets, Int. J. Refract. Met. Hard Mater. 24 (2006) 427–431. doi:10.1016/j.ijrmhm.2005.07.002.

[10] W. Midlands, Nickel in hardmetals, Met. Powder Rep. 48 (1993) 46. doi:10.1016/0026-0657(93)90317-l.

[11] A.M.F. Rocha, A.C. Bastos, J.P. Cardoso, F. Rodrigues, C.M. Fernandes, E. Soares, J. Sacramento, A.M.R. Senos, M.G.S. Ferreira, Corrosion behaviour of WC hardmetals with nickel-based binders, Corros. Sci. 147 (2019) 384–393. doi:10.1016/j.corsci.2018.11.015.

[12] E.A. Almond, B. Roebuck, Identification of optimum binder phase compositions for improved WC hard metals, Mater. Sci. Eng. 105–106 (1988) 237–248. doi:10.1016/0025-5416(88)90502-2.

[13] I.J. Shon, I.K. Jeong, I.Y. Ko, J.M. Doh, K. Do Woo, Sintering behavior and mechanical properties of WC-10Co, WC-10Ni and WC-10Fe hard materials produced by high-frequency induction heated sintering, Ceram. Int. 35 (2009) 339–344. doi:10.1016/j.ceramint.2007.11.003.

[14] E. Breval, J.P. Cheng, D.K. Agrawal, P. Gigl, M. Dennis, R. Roy, A.J. Papworth, Comparison between microwave and conventional sintering of WC/Co composites, Mater. Sci. Eng. A. 391 (2005) 285–295. doi:10.1016/j.msea.2004.08.085.

[15] H.C. Kim, D.Y. Oh, I.J. Shon, Sintering of nanophase WC-15vol.%Co hard metals by rapid sintering process, Int. J. Refract. Met. Hard Mater. 22 (2004) 197–203. doi:10.1016/j.ijrmhm.2004.06.006.

[16] A. Aramian, S.M.J. Razavi, Z. Sadeghian, F. Berto, A review of additive manufacturing of

cermets, Addit. Manuf. 33 (2020). doi:10.1016/j.addma.2020.101130.

[17] R.K. Enneti, K.C. Prough, T.A. Wolfe, A. Klein, N. Studley, J.L. Trasorras, Sintering of WC-12%Co processed by binder jet 3D printing (BJ3DP) technology, Int. J. Refract. Met. Hard Mater. 71 (2018) 28–35. doi:10.1016/j.ijrmhm.2017.10.023.

[18] R.K. Enneti, K.C. Prough, Wear properties of sintered WC-12%Co processed via Binder Jet 3D Printing (BJ3DP), Int. J. Refract. Met. Hard Mater. 78 (2019) 228–232. doi:10.1016/j.ijrmhm.2018.10.003.

[19] V.K. Balla, S. Bose, A. Bandyopadhyay, Microstructure and wear properties of laser deposited WC-12%Co composites, Mater. Sci. Eng. A. 527 (2010) 6677–6682. doi:10.1016/j.msea.2010.07.006.

[20] I. Konyashin, H. Hinners, B. Ries, A. Kirchner, B. Klöden, B. Kieback, R.W.N. Nilen, D. Sidorenko, Additive manufacturing of WC-13%Co by selective electron beam melting: Achievements and challenges, Int. J. Refract. Met. Hard Mater. 84 (2019). doi:10.1016/j.ijrmhm.2019.105028.

[21] E. Uhlmann, A. Bergmann, W. Gridin, Investigation on Additive Manufacturing of Tungsten Carbide.pdf, (n.d.).

[22] R.S. Khmyrov, V.A. Safronov, A. V. Gusarov, Synthesis of Nanostructured WC-Co Hardmetal by Selective Laser Melting, Procedia IUTAM. 23 (2017) 114–119. doi:10.1016/j.piutam.2017.06.011.

[23] S.L. Campanelli, N. Contuzzi, P. Posa, A. Angelastro, Printability and microstructure of selective laser melting of WC/Co/Cr powder, Materials (Basel). 12 (2019). doi:10.3390/ma12152397.

[24] S. Kumar, Process chain development for additive manufacturing of cemented carbide, J.

Manuf. Process. 34 (2018) 121–130. doi:10.1016/j.jmapro.2018.05.036.

[25] N. Ku, J.J. Pittari, S. Kilczewski, A. Kudzal, Additive Manufacturing of Cemented Tungsten Carbide with a Cobalt-Free Alloy Binder by Selective Laser Melting for High-Hardness Applications, Jom. 71 (2019) 1535–1542. doi:10.1007/s11837-019-03366-2.

[26] N. Kang, W. Ma, L. Heraud, M. El Mansori, F. Li, M. Liu, H. Liao, Selective laser melting of tungsten carbide reinforced maraging steel composite, Addit. Manuf. 22 (2018) 104–110. doi:10.1016/j.addma.2018.04.031.

[27] A.J. Cavaleiro, C.M. Fernandes, A.R. Farinha, C. V. Gestel, J. Jhabvala, E. Boillat, A.M.R. Senos, M.T. Vieira, The role of nanocrystalline binder metallic coating into WC after additive manufacturing, Appl. Surf. Sci. 427 (2018) 131–138. doi:10.1016/j.apsusc.2017.08.039.

[28] D. Gu, W. Meiners, Microstructure characteristics and formation mechanisms of in situ WC cemented carbide based hardmetals prepared by Selective Laser Melting, Mater. Sci. Eng. A. 527 (2010) 7585–7592. doi:10.1016/j.msea.2010.08.075.

[29] D. Gu, Q. Jia, Novel crystal growth of in situ WC in selective laser-melted W - C - Ni ternary system, J. Am. Ceram. Soc. 97 (2014) 684–687. doi:10.1111/jace.12828.

[30] C.W. Li, K.C. Chang, A.C. Yeh, J.W. Yeh, S.J. Lin, Microstructure characterization of cemented carbide fabricated by selective laser melting process, Int. J. Refract. Met. Hard Mater. 75 (2018) 225–233. doi:10.1016/j.ijrmhm.2018.05.001.

[31] H. Irrinki, M. Dexter, B. Barmore, R. Enneti, S. Pasebani, S. Badwe, J. Stitzel, R. Malhotra, S. V. Atre, Effects of Powder Attributes and Laser Powder Bed Fusion (L-PBF) Process Conditions on the Densification and Mechanical Properties of 17-4 PH Stainless Steel, Jom. 68 (2016) 860–868. doi:10.1007/s11837-015-1770-4.

[32] S.P. Narra, Z. Wu, R. Patel, J. Capone, M. Paliwal, J. Beuth, A. Rollett, Use of Non-Spherical Hydride-Dehydride (HDH) Powder in Powder Bed Fusion Additive Manufacturing, Addit. Manuf. 34 (2020). doi:10.1016/j.addma.2020.101188.

[33] T.W. Eagar, N.-S. Tsai, Temperature Fields Produced by Traveling Distributed Heat Sources, (1983). http://eagar.mit.edu/Publications/Eagar036.pdf (accessed January 15, 2018).

[34] L. Scime, J. Beuth, Melt pool geometry and morphology variability for the Inconel 718 alloy in a laser powder bed fusion additive manufacturing process, Addit. Manuf. 29 (2019) 100830. doi:10.1016/j.addma.2019.100830.

[35] M.J. Matthews, G. Guss, S.A. Khairallah, A.M. Rubenchik, P.J. Depond, W.E. King, Denudation of metal powder layers in laser powder bed fusion processes, Acta Mater. 114 (n.d.) 33–42. doi:10.1016/j.actamat.2016.05.017.

[36] ASTM, Standard Guide for Metallographic Sample Preparation of Cemented Tungsten, ASTM Stand. 08 (2012) 24–25. doi:10.1520/B0665-08.2.

[37] Astm, ASTM B276: Standard Test Method for Apparent Porosity in Cemented Carbides, ASTM Stand. (1996). doi:10.1520/B0276-91R96E01.

[38] ASTM E18/18M-11, Standard Test Methods for Rockwell Hardness of Metallic Materials, ASTM Int. (2018). doi:10.1520/E0018-17E01.

[39] J. Gockel, Integrated Control of Solidification Microstructure and Melt Pool Dimensions In Additive Manufacturing Of Ti - 6Al - 4V, Carnegie Mellon University, 2014. http://repository.cmu.edu/dissertations/374/.

[40] M. Tang, P.C. Pistorius, J.L. Beuth, Prediction of lack-of-fusion porosity for powder bed fusion, Addit. Manuf. 14 (2017) 39–48. doi:10.1016/j.addma.2016.12.001.

[41] W. Masaaki, Y. Akira, K. Akira, K. Kazuya, Spark Plasma Sintering of Binderless n-WC and n-WC- X (X = Nb , 39 (2010) 47–56.

[42] J. Yuan, Q. Zhan, J. Huang, S. Ding, H. Li, Decarburization mechanisms of WC-Co during thermal spraying: Insights from controlled carbon loss and microstructure characterization, Mater. Chem. Phys. 142 (2013) 165–171. doi:10.1016/j.matchemphys.2013.06.052.

[43] H.L. De Villiers Lovelock, Powder/Processing/Structure Relationships in WC-Co Thermal Spray Coatings: A Review of the Published Literature, J. Therm. Spray Technol. 7 (1998) 357–373. doi:10.1361/105996398770350846.

[44] C.J. Li, A. Ohmori, Y. Harada, Effect of powder structure on the structure of thermally sprayed WC-Co coatings, J. Mater. Sci. 31 (1996) 785–794. doi:10.1007/BF00367900.